nature materials

SUPPLEMENTARY INFORMATION

https://doi.org/10.1038/s41563-019-0348-x

In the format provided by the authors and unedited.

# Deterministic optical control of room temperature multiferroicity in $BiFeO_3$ thin films

**Yi-De Liou[1], Yu-You Chiu[1], Ryan Thomas Hart[2], Chang-Yang Kuo[3,4], Yen-Lin Huang[5], Yuan-Chih Wu[1], Rajesh V. Chopdekar[6], Heng-Jui Liu[7], Arata Tanaka[8], Chien-Te Chen[4], Chun-Fu Chang[3], Liu Hao Tjeng[3], Ye Cao[2], Valanoor Nagarajan[9], Ying-Hao Chu[5,10,11], Yi-Chun Chen[1,12]* and Jan-Chi Yang[1,12]***

[1]Department of Physics, National Cheng Kung University, Tainan, Taiwan. [2]Department of Materials Science and Engineering, University of Texas at Arlington, Arlington, TX, USA. [3]Max-Planck Institute for Chemical Physics of Solids, Dresden, Germany. [4]National Synchrotron Radiation Research Center, Hsinchu, Taiwan. [5]Department of Materials Science and Engineering, National Chiao Tung University, Hsinchu, Taiwan. [6]Advanced Light Source, Lawrence Berkeley National Laboratory, Berkeley, CA, USA. [7]Department of Materials Science and Engineering, National Chung Hsing University, Taichung, Taiwan. [8]Department of Quantum Matter, ADSM, Hiroshima University, Higashi-Hiroshima, Japan. [9]School of Materials Science and Engineering, University of New South Wales, Sydney, New South Wales, Australia. [10]Center for Emergent Functional Matter Science, National Chiao Tung University, Hsinchu, Taiwan. [11]Institute of Physics, Academia Sinica, Taipei, Taiwan. [12]Center for Quantum Frontiers of Research & Technology (QFort), National Cheng Kung University, Tainan, Taiwan. *e-mail: ycchen93@mail.ncku.edu.tw; janchiyang@phys.ncku.edu.tw

# SUPPLEMENTARY INFORMATION

## Deterministic optical control of room temperature multiferroicity in $BiFeO_3$ thin films

Yi-De Liou[1], Yu-You Chiu[1], Ryan Thomas Hart[2], Chang-Yang Kuo[3,4], Yen-Lin Huang[5], Yuan-Chih Wu[1], Rajesh V. Chopdekar[6], Heng-Jui Liu[7], Arata Tanaka[8], Chien-Te Chen[4], Chun-Fu Chang[3], Liu Hao Tjeng[3], Ye Cao[2], Valanoor Nagarajan[9], Ying-Hao Chu[5,10,11], Yi-Chun Chen[1,12]* and Jan-Chi Yang[1,12]*

[1] *Department of Physics, National Cheng Kung University, Tainan 70101, Taiwan*

[2] *Department of Materials Science and Engineering, University of Texas at Arlington, Arlington, TX 76019, USA*

[3] *Max-Planck Institute for Chemical Physics of Solids, Dresden 01187, Germany*

[4] *National Synchrotron Radiation Research Center, Hsinchu 30076, Taiwan*

[5] *Department of Materials Science and Engineering, National Chiao Tung University, Hsinchu 30010, Taiwan*

[6] *Advanced Light Source, Lawrence Berkeley National Laboratory, Berkeley, CA 94720, USA*

[7] *Department of Materials Science and Engineering, National Chung Hsing University, Taichung 402, Taiwan*

[8] *Department of Quantum Matter, ADSM, Hiroshima University, Higashi-Hiroshima 739-8530, Japan*

[9] *School of Materials Science and Engineering, University of New South Wales, Sydney 2052, Australia*

[10] *Center for Emergent Functional Matter Science, National Chiao Tung University, Hsinchu 30010, Taiwan*

[11] *Institute of Physics, Academia Sinica, Taipei 11529, Taiwan*

[12] *Center for Quantum Frontiers of Research & Technology (QFort), National Cheng Kung University, Tainan 70101, Taiwan*

*e-mail: ycchen93@mail.ncku.edu.tw and janchiyang@phys.ncku.edu.tw

**Figure S1 Ferroelectric polarization identification of light induced domains.**

Piezoresponse force microscopy (PFM) is employed to probe in-plane polarization directions of light induced domain structures. The IP ferroelectric domain structure is manifested by three contrasts, i.e., bright, dark, and intermediate, which represent the ferroelectric components with IP polarizations toward the left, the right, and along the axis of the cantilever, respectively. As shown in Fig. S1, the IP-PFM and IP-phase images of the same area were taken with sample rotation of $0^o$, $50^o$ and $90^o$ relative to the cantilever, respectively. Using this approach, the polarization of individual domain before and after light illumination could be revealed, as labeled with colored arrows in Fig. 2**a**.

Note: Fig. S1 shows the topography and PFM images of the mixed-phase BFO sample after laser illumination. The flat region in the topography image is tetragonal-distorted monoclinic BFO phase (T-BFO), while the mixed-phase stripes are composed of T-BFO and rhombohedral-distorted monoclinic BFO (R-BFO) phases. The PFM images show domain structures in the T-BFO region are periodic parallel patterns. The in-plane polarizations of T-BFO are along <100>pc series directions, with the domain wall lying along the <110>pc directions. The domain structures in the mixed-phase BFO region have special curved loops, where the R-BFO phases are enclosed inside the loops. The in-plane polarizations of R-BFO are along $<110>_{pc}$ series directions, with the strip T/R boundary lying close to the $<100>_{pc}$ directions, with about $10^o$ deviation.

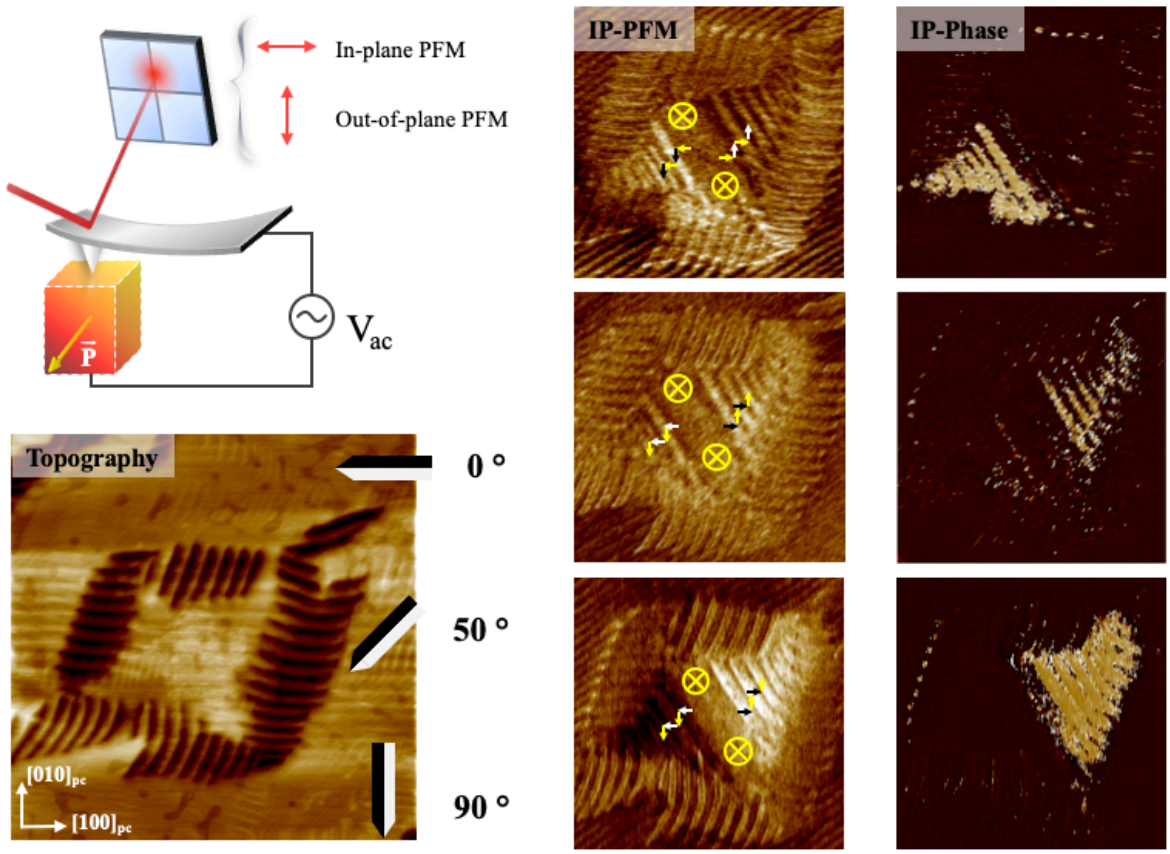


**Figure S2 Induced domains via different polarized light.**

The following figures show that the light-induced domain change under 0° , 45° , 90° linear polarized and circularly polarized light illumination, respectively. Our result indicates that the light induced domain patterns are similar regardless of the polarization of incident light.

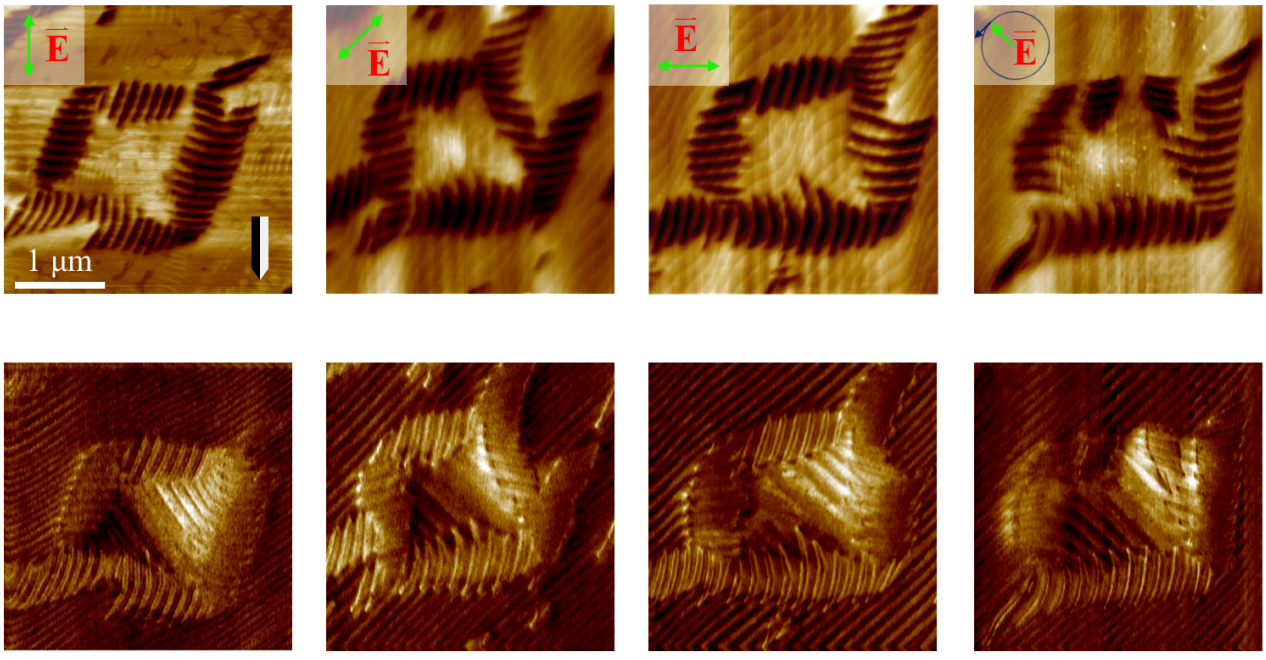

**Figure S3 Ultraviolet–visible spectroscopy and Photoluminescence spectroscopy of mixed phase $BiFeO_3$ films.**

In addition to the light-induced flexoelectric effect that could contribute to the non-volatile optical control of mixed phase BFO system, the mechanism related to free-carrier-generation-induced photocurrent[1] or deformation[2] must be considered. Fig. S3**a** shows the UV spectra of our BFO thin film. The measured BFO band gap of ~ 2.74 eV indicates the film does not show a band gap extending to the range of the 532 nm green laser. Additionally, no photoluminescence signals related to defect states are observed when the BFO sample is illuminated by the 532 nm laser, as shown in the Fig. S3**b**. As a result, the illumination of a 532 nm laser will not generate significant amount of photo-excited carriers to drive the rotation of the ferroelectric polarization or to deform the strain-sensitive BFO lattice.

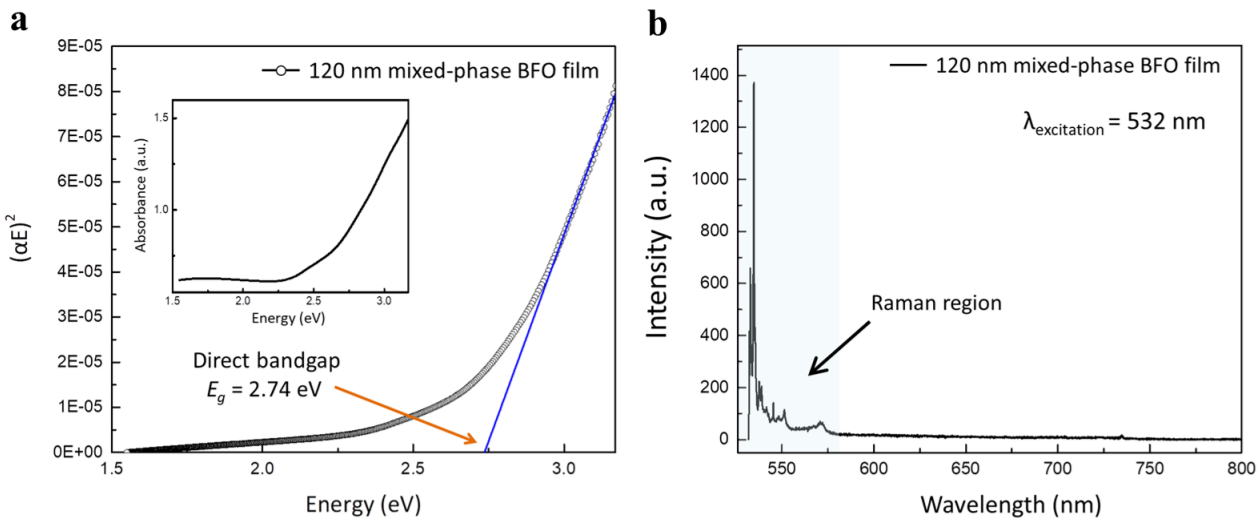

**Figure S4 Temperature dependent reciprocal space maps (RSMs) of T-like BFO phase.**

The phase transition of the T-like BFO phase is confirmed by RSMs around the BFO (103) reflections collected at Fig. S4**a** room temperature (RT) and Fig. S4**b** 150 °C using a synchrotron based high–resolution 8 circle diffractometer at beamline BL-17B1 at the National Synchrotron Radiation Research Center (NSRRC) in Hsinchu, Taiwan. In the RSM at RT, BFO exhibits a threefold split of diffraction pattern, which is a typical feature for monoclinic $M_C$ symmetry as the schematic shown in Fig. S4**c**. When temperature increases to 150 °C the pattern changes to a two-fold split at the same reflection zone, which becomes a typical feature for monoclinic $M_A$ symmetry as the schematic shown in Fig. S4**d**. The obvious variation of the diffraction patterns concludes that the monoclinic shear angle is along the *a*-axis of BFO at RT, and then moves to the in-plane diagonal direction of BFO at 150 °C confirming the $M_C \rightarrow M_A$ phase transition as the schematic shown in Fig. S4**e**.

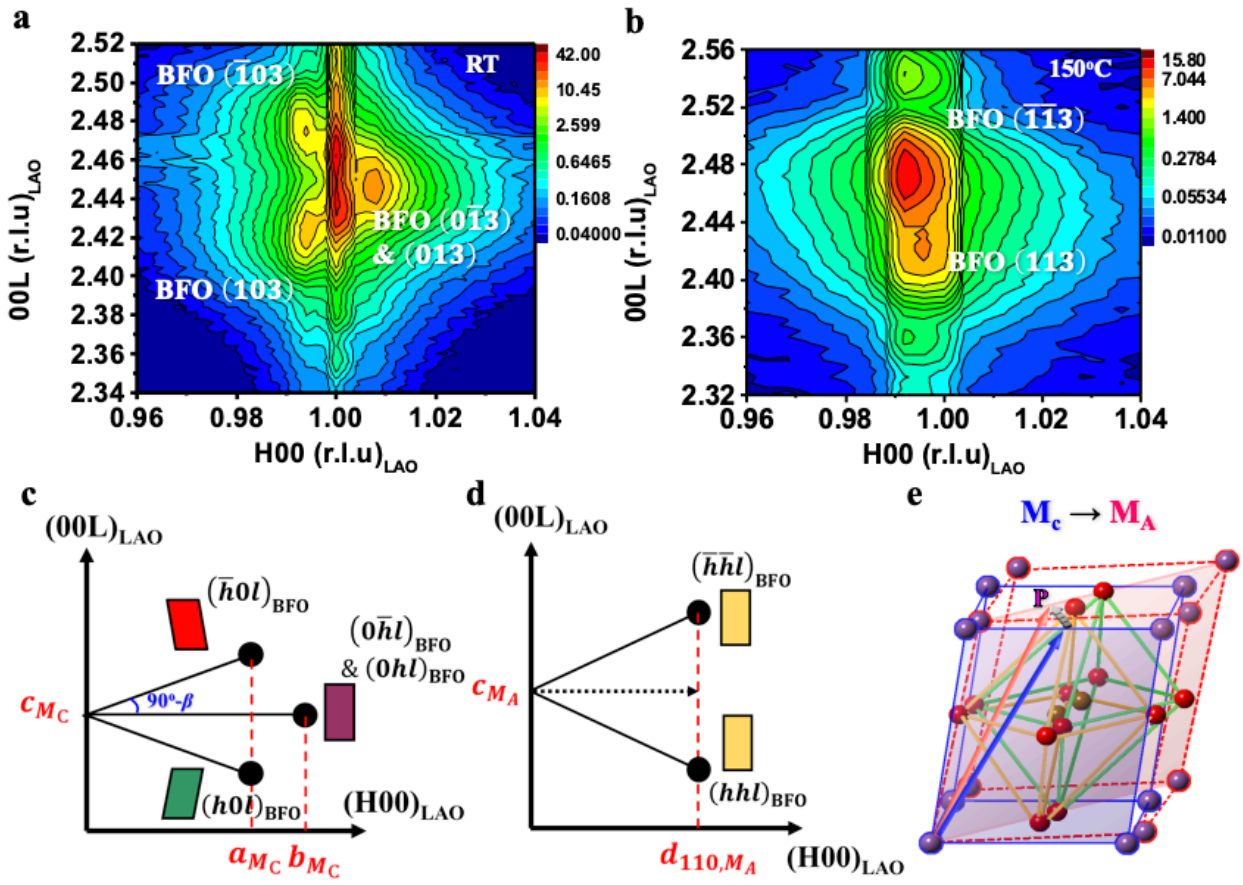

**Figure S5 Detailed fitting of power dependent Raman spectrum of T-like BFO phase.**

In this part we deal with the detailed fitting of Fig. 3**a** in the main text. The optical phonon mode at 364 and 390 $cm^{-1}$ are assigned to the phonons of T-like BFO phase, which is consistent to previous researches[3]. Each spectrum is fitted by Lorentz function and then normalized to the intensity of phonon mode at 390 $cm^{-1}$. The weakened trend of phonon mode at 364 $cm^{-1}$ under the 15.9 $mW/\mu m^2$ illumination clearly indicates the sign of structure phase transition. Through careful comparison between temperature and power dependent Raman spectra, we deduced that the illumination of laser density of 15.9 $mW/\mu m^2$ corresponds to the local heating ~ 150 $^oC$.

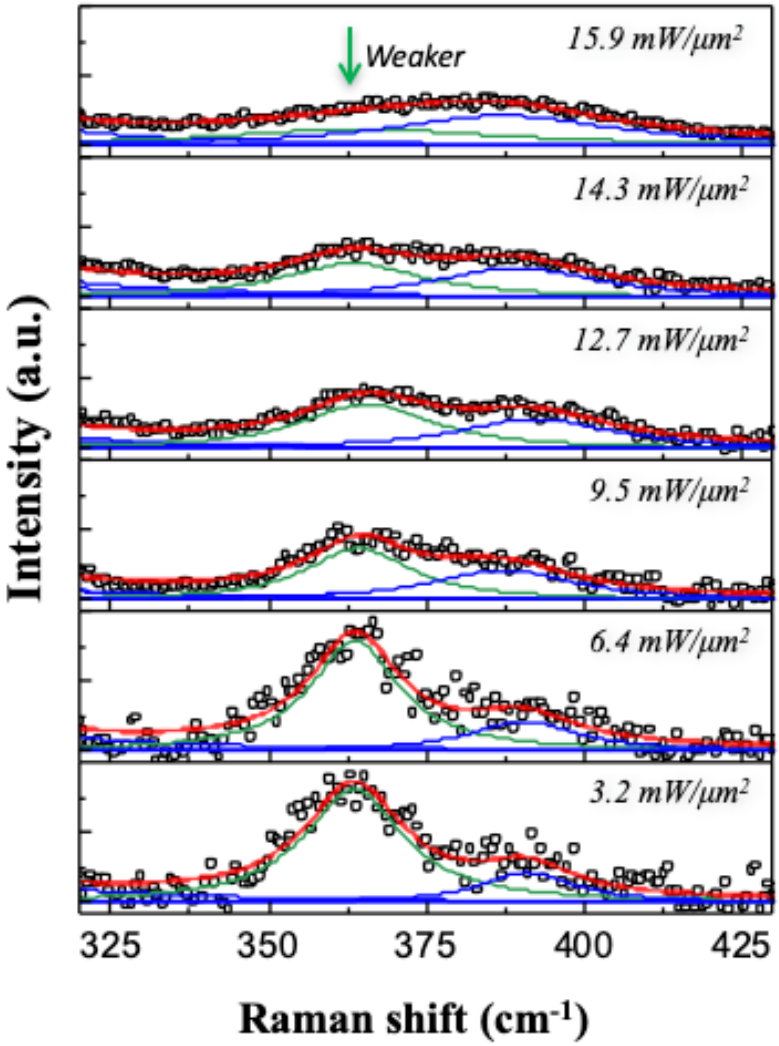

**Figure S6 Local temperature determination via the analysis of Stokes/Anti-stokes ratio.**

The laser-induced heating effect could be controlled by adjusting the power density of the laser. Through the analysis of the Stokes/anti-Stokes Raman spectra, local temperature could be deduced. As shown in the schematic of Fig. S6**a**, the inelastic scattering process of the Stokes part differs from that of the Anti-stoke part in the initial state. The expected number of phonons as a function of energy state and temperature is described by the Bose–Einstein statistics. The ratios of Stokes and anti-Stokes Raman intensities follow the equation[4]:

$$I_S / I_{AS} = \frac{(v_{excitation} - v_{phonon})^3}{(v_{excitation} + v_{phonon})^3} \exp[h v_{phonon} / kT]$$

where $\nu_{excitation}$ is the frequency of the excitation laser, and $\nu_{excitation} \pm \nu_{phonon}$ are the frequency of Raman Stokes ( –) and anti-Stokes (+) peaks. The 1st part of the equation is due to the cube frequency dependence of the scattering cross-section of inelastic Stokes and anti-Stokes Raman processes, while the exponential dependence with temperature in the 2nd part is due to the relative occupation of the ground and excited states based on the Boltzmann distribution.

The Stokes/anti-Stokes Raman results are shown in Fig. S6**b**. The optical phonon mode at 690 $cm^{-1}$ (assigned to the phonon of T-like BFO phase[3]) is adopted to determine the local temperature due to its notable spectrum characteristics, including high signal-to-noise ratio, far away from laser background and clear peak feature. We could observe that the intensity of anti-Stokes Raman band of phonon mode at 690 $cm^{-1}$ increases with increasing laser power density. After fitted by Lorentz area function, the local temperature induced by laser heating is obtained. An estimated value of 152 ° C under a 15.9 $mW/\mu m^2$ illumination is deduced, which is the structure phase transition temperature of T-BFO. The detailed information including Stokes/anti-Stokes ratios and corresponding temperatures are illustrated in Fig. 3**d**, in which the error bar varies with different signal-to-noise based on its illumination condition.

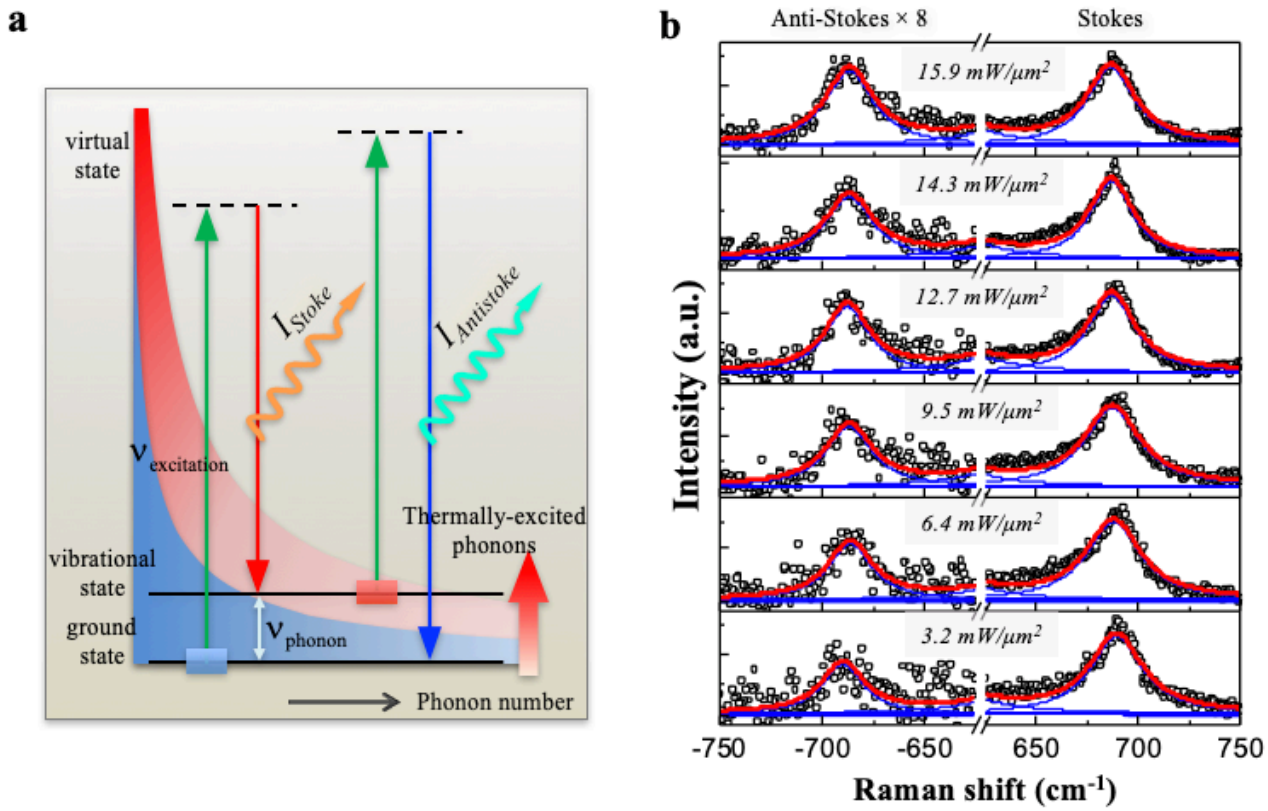


**Figure S7 The 532 nm laser intensity profile measured by laser beam profiler.**

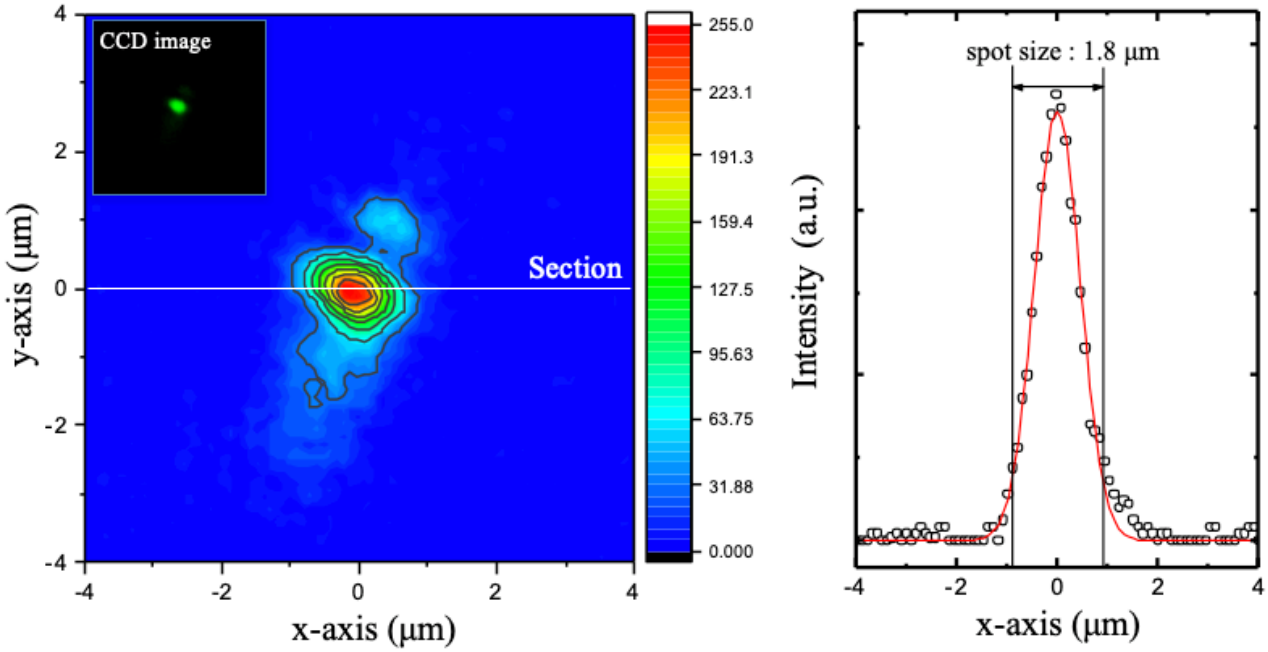

**Figure S8 Phase-field simulation based on dome-like strain/stress distribution in the illuminated area.**

**a**, The light-induced out-of-plane stress ($\sigma_{33}$) distribution **b**, in-plane flexoelectric field along *x* direction, **c**, in-plane flexoelectric field along *y* direction on the top surface of BFO thin film (flexoelectric coefficient $f_{ij}$ = 10V), which are maximized at the boundaries between the illuminated and unilluminated regions and, **d**, a schematic plot of the dome-like stress distribution. e, 3-dimensional and **f**, the corresponding top surface of the simulated domain structure under the light illumination, showing the net in-plane polarization orientations along $[110]_{pc}$ and $[\bar{1}\bar{1}0]_{pc}$ in the top-right and bottom-left sections of the illuminated region.

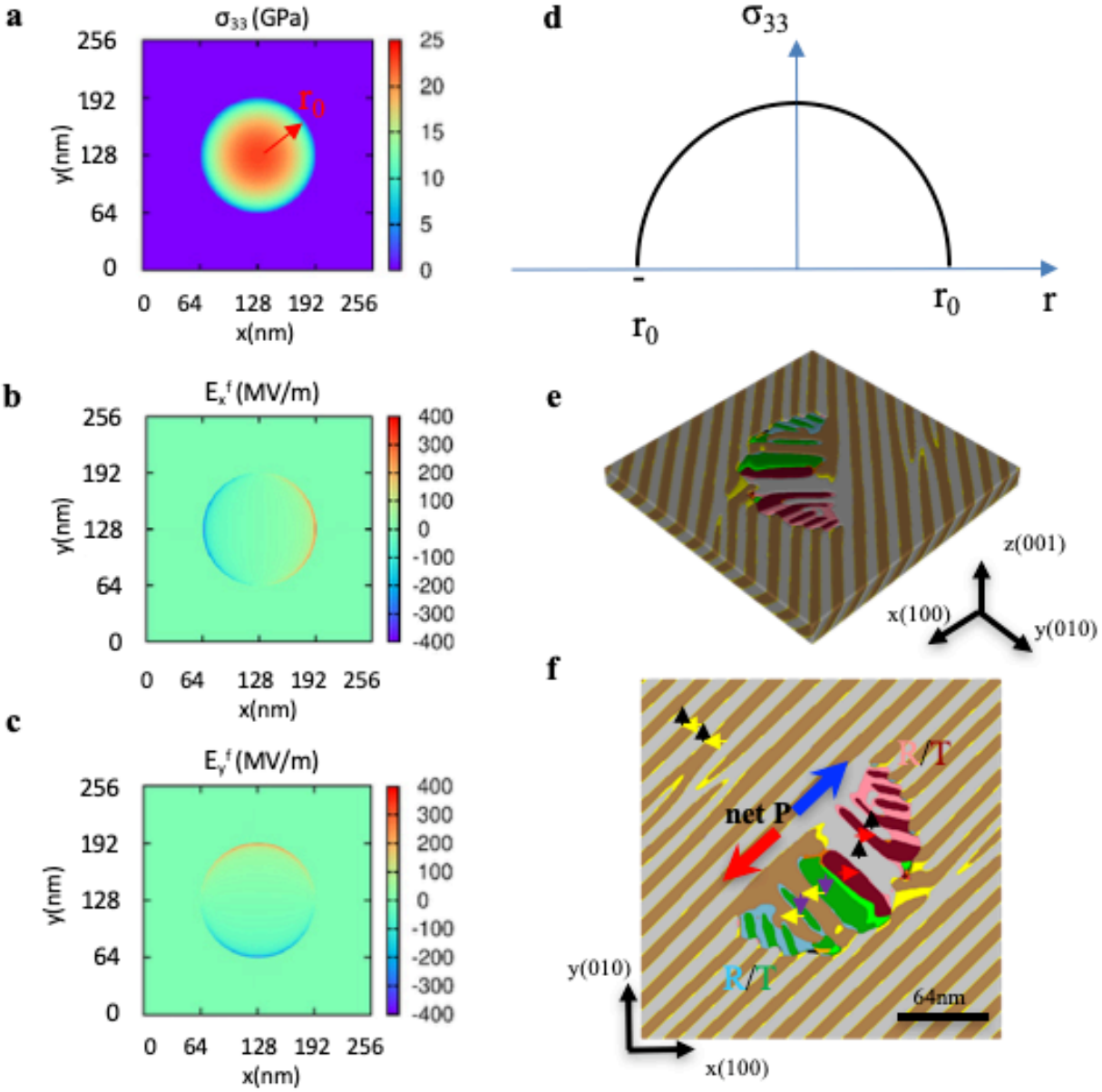

**Figure S9 Phase-field simulation of BFO ferroelectric domains under different temperatures and flexoelectric field directions.**

Fig. S9 shows the phase-field simulation of BFO domain structure under different effective directions of flexoelectric field ($E^f$). **a**, Equilibrium domain structure before illumination; **b**, under illumination with uniform $E^f$ along the $[\bar{1}10]_{pc}/[1\bar{1}0]_{pc}$ directions in the upper-left/lower-right triangles of the illuminated region; **c**, the equilibrium domain structure when the flexoelectric field illustrated in **b** is reduced to 0 (after illumination), which shows no formation of the new T phase domain patterns. **d**, Phase-field simulation of BFO under illumination with uniform $E^f$ along the $[110]_{pc}/[\bar{1}\bar{1}0]_{pc}$ directions in the upper-right/lower-left triangles of the illuminated region; **e**, the equilibrium domain structure when the flexoelectric field illustrated in **d** is reduced to 0 (after illumination), where new domain pattern is seen and becomes stable in the illuminated region. These simulation results nicely support the experimental observation as discussed in the main text.

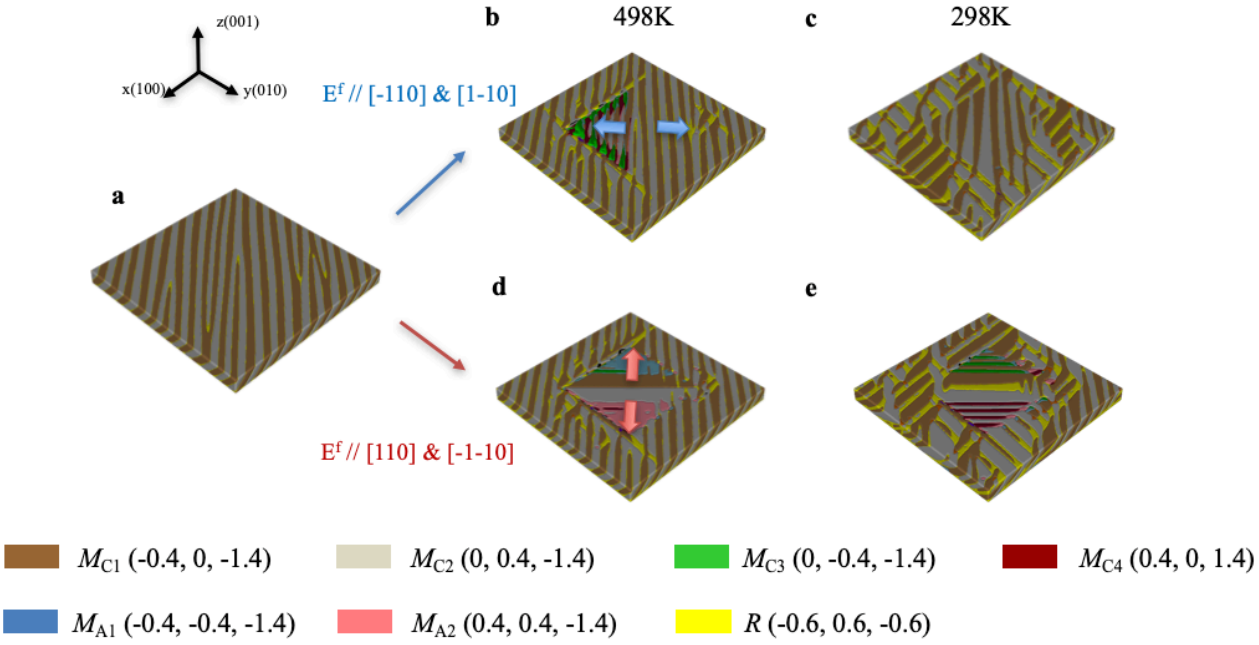

**Figure S10 Phase-field simulation with smaller flexoelectric coefficient ($f_{ij}$ = 1V).**

**a**, The light-induced out-of-plane stress ($\sigma_{33}$) distribution, **b**, in-plane flexoelectric field along *x* direction, **c**, in-plane flexoelectric field along *y* direction on the top surface of BFO thin film ($f_{ij}$ = 1V) and **d**, a schematic plot of the dome-like stress distribution; **e**, 3-dimensional and **f**, the corresponding top surface of the simulated domain structure under the light illumination. No polarization rotations and new pattern formation are observed due to smaller flexoelectric strength.

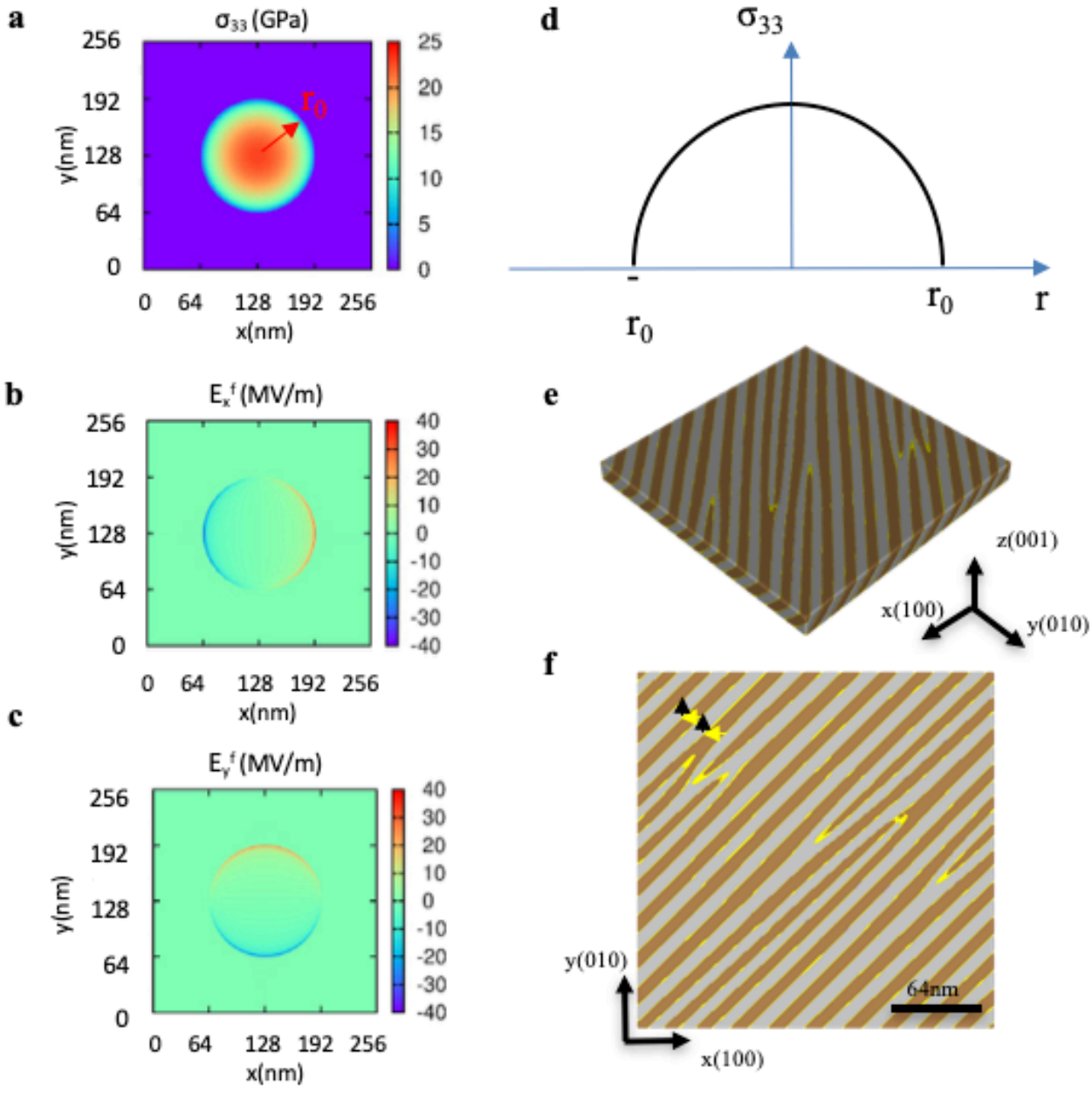

**Figure S11 X-ray linear dichroism study on mixed-phase BFO.**

X-ray absorption spectroscopy (XAS) studies were performed at TPS45A NSRRC-MPI beamline at Taiwan Photon Source (TPS). To explore the difference of the magnetic properties between the T-BFO and the R-BFO thin films, we measured at the room temperature the polarization dependent X-ray absorption spectroscopy (XAS) at Fe $L_{2,3}$-edge with the incident beam 20° off the film surface and varied the light polarization from vertical to horizontal polarization. The measured geometry is depicted in Fig. S11**a**, and the experimental results are presented in Fig. S11**b-e**. The red lines were collected with the **E** vector of the incident light perpendicular to ***c***-axis, defined as LV, and the blue lines for **E** parallel to the axis 20° away from ***c***-axis (see in Fig. S11**a**), defined as LH. The linear dichroism spectra, defined as LV– LH, are also presented as the brown dots in Fig. S11**b-e**. Clear line shape differences, both in XAS and dichroism spectra, between the T-BFO and the R-BFO thin films are observed, indicating a different anti-ferromagnetic axis[5-7].

To further extract the magnetic information from the experimental spectra, we simulated the XAS spectra by performing the configuration interaction cluster calculations. This theoretical approach includes the full atomic multiplet theory and the local effects of the solid[8-10]. The calculations were done using the program XTLS 8.3[9]. This well established configuration interaction cluster model is being well proven to determine the anti-ferromagnetic axis and its transition temperature from anti-ferromagnetic systems[5-7]. The calculated polarization dependent spectra are shown just below the experimental spectra in Fig. S11**b-e**, and the calculated dichroism spectra are presented as the green lines. Parameters used in the calculations are listed in ref.[11]. Two anti-ferromagnetic axes, that are perpendicular to the ***c***-axis and orthogonal to each other, were taken into account[7,12]. The magnetic exchange interaction between two $Fe^{3+}$ ions was taken into account as a fitting parameter of $H_{ex}$ (magnetic exchange energy). We found that for the T-BFO the experimental XAS spectra as well as the dichroism spectrum can be nicely reproduced by the calculation with $H_{ex}$= 0 meV, whereas for the R-BFO $H_{ex}$ needs to be as large as 25 meV, see the comparisons in Fig. S11**b-e**. This result directly points out that the Néel temperature, $T_N$, of the T-BFO thin film is much lower than that of the R-BFO thin film, and is close to the room

temperature as suggested in Ref. [13]. This corroborates that the stronger contrast area in the XLD-PEEM image is from the R-BFO among the mixed phase stripes after laser illumination. Conclusively, our findings demonstrate that the magnetic properties of mixed phase BFO thin films can be manipulated by the proposed optical means.

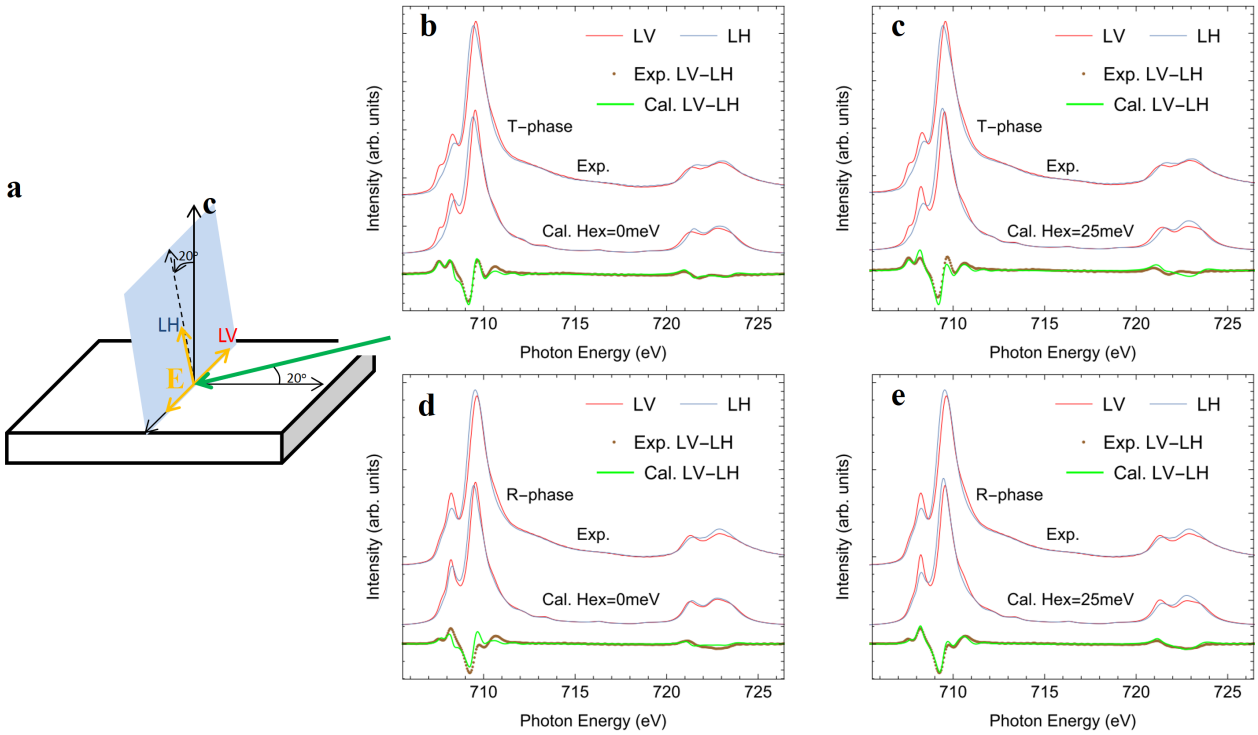


**Soft X-ray polarization dependent spectra at Fe $L_{2,3}$-edges. a**, The experimental geometry where the incidence beam is depicted as a green arrow and the yellow arrows for the **E** of the light. **b-e**, Experimental and calculated spectra for the T-phase (**b**,**c**) and R-phase (**d**,**e**) of $BiFeO_3$ thin film.

**Figure S12 Deterministic control of conductivity in mixed-phase BFO.**

The non-volatile conduction modulation of mixed-phase BFO is achieved by controlling the motion of illuminated laser, as characterized by the conductive atomic force microscopy (C-AFM). Fig. S12**a** shows the as-grown current image as well as the cross-section current profile, identifying the obvious conductivity at the mixed-phase stripes, which is nicely consistent with previous studies[14,15]. Fig. S12**b** shows a demonstration of light-modulated current states by tailoring the switching between T-BFO matrix and mixed phase patterns in the same area. State 1 shows the low-conduction state composed of as-grown T-BFO, which is then transformed to conductive mixed-phase stripes under light illumination (state 2). The conductive mixed-phase stripes could once again be converted back to pure T-BFO matrix showing negligible conductance (state 3). This demonstration successful validates the reversible control of the conductance in multiferroic BFO by means of light.

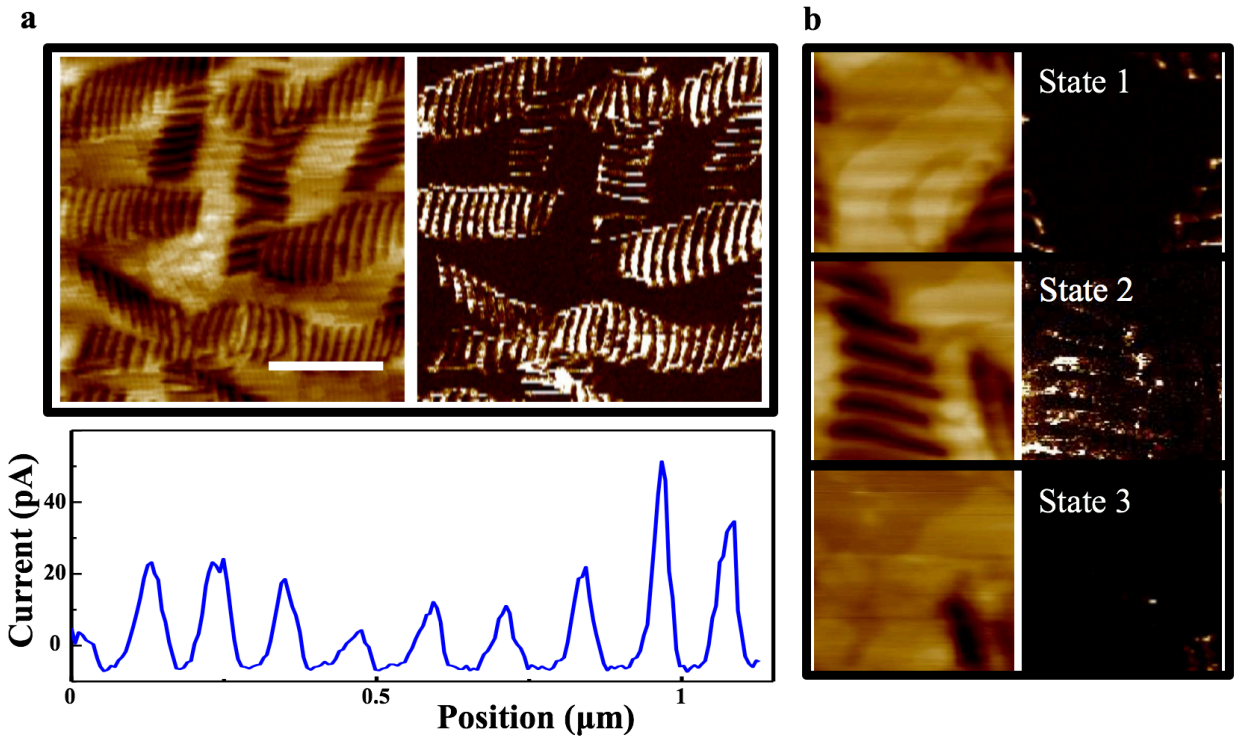

**Supplementary References**


1. Yang, M. M. & Alexe, M. Light-induced reversible control of ferroelectric polarization in $BiFeO_3$. *Adv. Mater.* **30**, 1704908 (2018).
2. Paillard, C. *et al.* Photovoltaics with ferroelectrics: Current status and beyond. *Adv. Mater.* **28**, 5153-5168 (2016).
3. Huang, Y. C. *et al.* Magnetic-coupled phase anomaly in mixed-phase $BiFeO_3$ thin films. *APL Mater.* **5**, 086112 (2017).
4. Kip, B. J. & Meier, R. J. Determination of the local temperature at a sample during Raman experiments using Stokes and anti-Stokes Raman bands. *Appl Spectrosc.* **44**, 707-711 (1990).
5. Kuiper, P., Searle, B. G., Rudolf, P., Tjeng, L. H. & Chen, C. T. X-ray magnetic dichroism of antiferromagnet $Fe_2O_3$ : The orientation of magnetic-moments observed by fe 2*p* x-ray absorption-spectroscopy. *Phys. Rev. Lett.* **70**, 1549-1552 (1993).
6. Kuo, C. Y. *et al.* $k$=0 magnetic structure and absence of ferroelectricity in $SmFeO_3$. *Phys. Rev. Lett.* **113**, 217203 (2014).
7. Kuo, C. Y. *et al.* Single-domain multiferroic $BiFeO_3$ films. *Nat. Commun.* **7**, 12712 (2016).
8. Degroot, F. M. F. X-ray-absorption and dichroism of transition-metals and their compounds. *J. Electron Spectrosc. Relat. Phenom.* **67**, 529-622 (1994).
9. Tanaka, A. & Jo, T. Resonant 3*d*, 3*p* and 3*s* photoemission in transition-metal oxides predicted at 2*p* threshold. *J. Phys. Soc. Jpn.* **63**, 2788-2807 (1994).
10. Bocquet, A. E. *et al.* Electronic structure of early 3*d*-transition-metal oxides by analysis of the 2*p* core-level photoemission spectra. *Phys. Rev. B* **53**, 1161-1170 (1996).
11. $\Delta$=2.0 eV, $U_{dd}$=5.0 eV, $U_{pd}$=6.0 eV, Slater integrals reduced to 70% of Hartree-Fock values, pdσ = -1.47 eV, pdπ = 0.68 eV, 10Dq = 0.5 eV for R-phase, 10Dq = 0.6 eV for T-phase, $\Delta_{eg}$=0.22 eV for R-phase, $\Delta_{eg}$=0.30 eV for T-phase, $\Delta_{t2g}$=-0.12ev for R-phase, $\Delta_{t2g}$=-0.30 eV for T-phase.
12. Sando, D. *et al.* Crafting the magnonic and spintronic response of $BiFeO_3$ films by epitaxial strain. *Nat. Mater.* **12**, 641-646 (2013).
13. Ko, K. T. *et al.* Concurrent transition of ferroelectric and magnetic ordering near room temperature. *Nat. Commun.* **2**, 567 (2011).
14. Chu, K. *et al.* Enhancement of the anisotropic photocurrent in ferroelectric oxides by strain gradients. *Nat. Nanotech.* **10**, 972-979 (2015).
15. Seidel, J. *et al.* Electronic properties of isosymmetric phase boundaries in highly strained Ca-doped $BiFeO_3$. *Adv. Mater.* **26**, 4376-4380 (2014).